

Article

Facile Synthesis of Visible Light-Induced g-C₃N₄/Rectorite Composite for Efficient Photodegradation of Ciprofloxacin

Zhiming Sun ^{1,*} , Xiangwei Zhang ¹, Rui Zhu ¹, Xiongbo Dong ¹, Jie Xu ¹ and Bin Wang ^{2,*}

¹ School of Chemical and Environmental Engineering, China University of Mining and Technology (Beijing), Beijing 100083, China; zhangxiangwei0613@126.com (X.Z.); 13121969011@163.com (R.Z.); 18810672030@163.com (X.D.); 13126852095@163.com (J.X.)

² Beijing Key Laboratory of Clothing Materials R&D and Assessment, Beijing Engineering Research Center of Textile Nanofiber, School of Materials Science and Engineering, Beijing 100029, China

* Correspondence: zhimingsun@cumt.edu.cn (Z.S.); 20150010@bift.edu.cn (B.W.); Tel.: +86-10-62339920 (Z.S.)

Received: 8 September 2018; Accepted: 30 November 2018; Published: 3 December 2018



Abstract: A novel kind of g-C₃N₄/rectorite composite with high visible-light photoactivity was developed via a mild and cost effective two-step process. Ciprofloxacin (CIP), a typical antibiotic, was applied to evaluate the photoactivity of the received catalyts. Furthermore, the by-products of CIP photodegradation were analyzed and the possible degradation pathways were also discussed. Compared with bare photocatalysts, the received composite possessed well reusability and higher photoactivity towards CIP. According to the characterization analysis results, layered g-C₃N₄ was successfully immobilized on layered rectorite, which could not only promote its adsorption capacity but also provide more reactive sites for CIP adsorption and photodegradation. Compared with bare g-C₃N₄, the photoactivity of the prepared composite was significantly enhanced. The enhancement should be mainly due to the lower recombination rate of photogenerated carriers and the improved adsorption capacity toward CIP. This study demonstrated that the obtained g-C₃N₄/rectorite composite should be a promising alternative material in wastewater treatment.

Keywords: rectorite; g-C₃N₄; photocatalysis; ciprofloxacin; wastewater treatment

1. Introduction

With the fast development of industry, a large volume of wastewater, particularly, the residuals of medicine such as ciprofloxacin (CIP) are excreted into the ground waters, which seriously threaten the existence and long-term development of human society due to their biotoxicity and refractory [1]. To address these issues, traditional solutions such as ultrafiltration [2], absorption [3,4] and biological treatment [5] have been widely applied. However, these traditional methods could not effectively eliminate and completely mineralize the CIP. In recent years, many researches have been investigated to explore an environmentally friendly and renewable technology to degrade these medicines. Among these reported technologies, photocatalysis has been proven to be a green and efficient route to resolve the environmental problems on account of its low production cost and easy-to-operate. Particularly, TiO₂ as a photocatalytic material has gained considerable interests, which exhibits enormous application prospect in photocatalysis [6]. However, the practical application of the bare anatase TiO₂ nanoparticles was limited to a certain extent due to their relatively higher band gap (around 3.2 eV). Compared with TiO₂ nanoparticles, the band gap of g-C₃N₄ is lower (around 2.7 eV), leading to its preferable visible light-induced photoactivity in water splitting and removal of various contaminants [7]. Additionally, g-C₃N₄ could be simply synthesized by heating some nitrogen containing compounds, for example cyanamide [8], dicyandiamide [9], trithiocyanuric acid [10],

melamine [11], triazine [12], heptazine derivatives [13], urea [14] and thiourea [15], which means that the preparation methods of $g\text{-C}_3\text{N}_4$ would be easy to operate and inexpensive. However, $g\text{-C}_3\text{N}_4$ photocatalyst would easily agglomerate in the process of thermal polycondensation, leading to the decrease in the active sites of the adsorption towards pollutant.

To solve these application problems of $g\text{-C}_3\text{N}_4$, a great number of methods have been reported, such as exfoliating the bulk $g\text{-C}_3\text{N}_4$ by using organic solvents, acid media, or base media [16]. Due to their high-cost and environmentally unfriendly defects, these above methods could not be widely used in practical application. In recent years, some natural minerals with unique lamellar structure, such as kaolinite [17], montmorillonite [18], illite [19] and so forth, have been widely used as the $g\text{-C}_3\text{N}_4$ carriers to hinder the agglomeration of $g\text{-C}_3\text{N}_4$ during the thermal polycondensation process. Among these natural layered minerals, the rectorite seems to be an attractive option as catalyst carrier to synthesized 2D/2D hierarchical structure. On one hand, rectorite has a regular interstratified structure consist of 1:1 ratio of a mica component and a montmorillonite component, so the properties of rectorite were similar to both mica and montmorillonite. On the other hand, it has relatively higher thermal stability, compared with the other natural layered minerals, which would maintain the structure stability during the thermal polycondensation process of $g\text{-C}_3\text{N}_4$ [20,21].

Hence, in our present study, a novel $g\text{-C}_3\text{N}_4$ /rectorite composite was developed via a facile and cost-effective route. Ciprofloxacin (CIP) was selected as the typical contaminant to evaluate the photoactivity of samples. The possible degradation pathway was illustrated based on the ESI-MS results. In addition, the possible photodegradation mechanism was discussed based on the scavenger experiment results as well. This paper would provide new insight for natural layered mineral based composite photocatalysts and a fundamental understanding of $g\text{-C}_3\text{N}_4$ /rectorite composite to degrade wastewater.

2. Materials and Methods

2.1. Materials

The rectorite (RE) used in the study was obtained from Zhongxiang city, Hubei province, China, which was used as the carrier of $g\text{-C}_3\text{N}_4$. Deionized water was applied to the whole experiment. Dicyandiamide ($\text{C}_2\text{H}_4\text{N}_4$), ciprofloxacin (CIP) and other chemicals were purchased from Beijing Reagent Co. (Beijing, China). All chemicals used in this study were analytical grade without any further purification.

2.2. Catalysts Preparation

The bare $g\text{-C}_3\text{N}_4$ was obtained from a typical thermal polycondensation process of dicyandiamide [22]. Typically, 4.0 g dicyandiamide was put into an alumina crucible with a cover and heated to 550 °C in open air for 4 h at a heating rate of 2.3 °C·min⁻¹. The resultant yellow product was collected for use without any further treatment. As a reference, the rectorite was also calcined at 550 °C (RE-550 °C) as same as the synthesis of bare $g\text{-C}_3\text{N}_4$ catalyst.

The $g\text{-C}_3\text{N}_4$ /rectorite catalyst was prepared by a facile two-step process consisted of wet-chemical and calcination processes. In a typical synthesis, different qualities (1.0 g, 2.0 g, 3.0 g and 4.0 g) of dicyandiamide were dispersed into 60 mL of deionized water at 60 °C, while the solution was stirred continually. Afterwards, 1.0 g of rectorite was dissolved into above solution and stirred continually for 12 h. The resulted suspension was then treated at 105 °C for 10 h. Finally, the product was treated under the same thermal conditions as bare $g\text{-C}_3\text{N}_4$. The composites were designated as CNRE-1:1, CNRE-1:2, CNRE-1:3 and CNRE-1:4, respectively. According to the thermogravimetric analysis (TG), the mass ratio of $g\text{-C}_3\text{N}_4$ was measured as 65.4% in CNRE-1:3.

2.3. Characterization

The crystalline phase and structure were studied by X-ray powder diffraction (XRD) (Bruker, Karlsruhe, Germany) with Cu-K α radiation ($\lambda = 0.154056$ nm). The surface character and morphology of samples were investigated by the S-4800 scanning electron microscopy (SEM) (Hitachi, Tokyo, Japan) equipped with an energy dispersive spectrum analysis (EDS). Photoluminescence (PL) spectra of as-prepared photocatalysts were received through the use of a fluorescence spectrophotometer (F-7000 PL) (Hitachi, Tokyo, Japan) with an emission wavelength of 360 nm. Fourier transformed infrared (FTIR) spectra was performed on a Nicolet iS10 spectrometer (Thermo Fisher Scientific, Waltham, MA, America) in the frequency range of 4000 and 600 cm^{-1} . The reflectance spectra of as-prepared photocatalysts with the scope from 200 nm to 800 nm were measured by a UV-vis spectrophotometer (UV-9000s, Shanghai Metash Instruments Co., Shanghai, China), which equipped with the diffuse reflectance accessory (DRS). The BET surface area and pore size distribution was assessed by JW-BK nitrogen adsorption-desorption isotherm analyzer apparatus (JWGB Sci. &Tech, Beijing, China) at 77 K.

2.4. Evaluation of Photocatalytic Activity

The photodegradation of CIP was carried out to measure the photoactivity. The visible light system was consisted of a 500 W Xenon lamp (BL-GHX-V, Shanghai Bilang plant, Shanghai, China) with a 420 nm cut-off filter to prevent the UV light from passing through. In the degradation experiment, 50 mg of sample (g-C₃N₄, CNRE-1:1, CNRE-1:2, CNRE-1:3 and RE) was added into the CIP solution (50 mL, 20 mg/L). As an object of comparative experiment, a physical mixture of rectorite and g-C₃N₄ was used to evaluate the photoactivity as well. The content of g-C₃N₄ in mixture was set as 65.4% (CNRE-MIX), same as CNRE-1:3. Subsequently, the ultrasonic vibration was used to make the suspension more uniformly. Then the mixture was transferred to the cylindrical reactor. Before the visible light illumination, the mixture was stirred without visible light for 30 min and then the catalysts and CIP would establish an adsorption/desorption equilibrium. At regular intervals, 4 mL of mixture was removed from the cylindrical reactor and centrifuged at 8000 rpm to separate pollutant and photocatalyst. An UV-vis spectrophotometer (UV-9000S, Shanghai Metash, Shanghai, China) was applied to monitor the removal performance for CIP. The maximum absorption of CIP was measured at 278 nm. Using the following formula, the degradation rate of CIP (D_R) was evaluated:

$$D_R = (C_0 - C_t)/C_0 \times 100\% \quad (1)$$

where, C_0 represents the concentration of CIP at initial time and C_t represents the concentration at time t . All the experiments were repeated for two times.

2.5. Analysis of Degradation by-Products of CIP

The photocatalytic mechanism was proposed by investigating the decomposition pathway of CIP. The possible intermediates from CIP degradation were determined using electrospray ionization mass spectrometry (ESI-MS, micrOTOF-Q II, Bruker, Karlsruhe, Germany). Full-scan spectra were measured by m/z scanning from 50 to 1000. The capillary voltage was set at 3000 V. The collision cell RF was set at 110.0 Vpp. The pressure of the nebulizer was set at 0.4 bar. The temperature of the dry heater was set at 180 °C. The flow rate of the dry gas was controlled at 2.0 L min^{-1} .

3. Results and Discussion

3.1. XRD Analysis

The crystallographic and structural characteristics of rectorite, g-C₃N₄ and CNRE-1:3 were present in Figure 1. It is clear that rectorite displays two relative strong peaks at 7.25° and 28.89°, which could be indexed as the (002) and (008) lattice plane, respectively. This is well matched with the patterns

of rectorite (JCPDS No. 29-1495) [23,24]. Other several peaks located at 17.88° , 20.04° and 35.40° are assigned to (005), (100) and (113) lattice planes, respectively. The peak at 12.47° represented the existence of the kaolinite in this sample [25]. In addition, the typical diffraction peaks of impurity rutile at 27.49° , 36.14° , 54.40° , 62.61° were also observed in rectorite [26]. Two peaks located at 13.08° and 27.58° are observed in $g\text{-C}_3\text{N}_4$, which are the characteristic peaks of $g\text{-C}_3\text{N}_4$. The stacking of $g\text{-C}_3\text{N}_4$ layers attribute to the diffraction peak at 27.58° (002) and diffraction peak at 13.08° (100), which could be assigned to the period structural of triazine units [22]. Simultaneously, these two diffraction peaks also appeared in the XRD pattern of CNRE-1:3, demonstrating that $g\text{-C}_3\text{N}_4$ was successfully immobilized on rectorite.

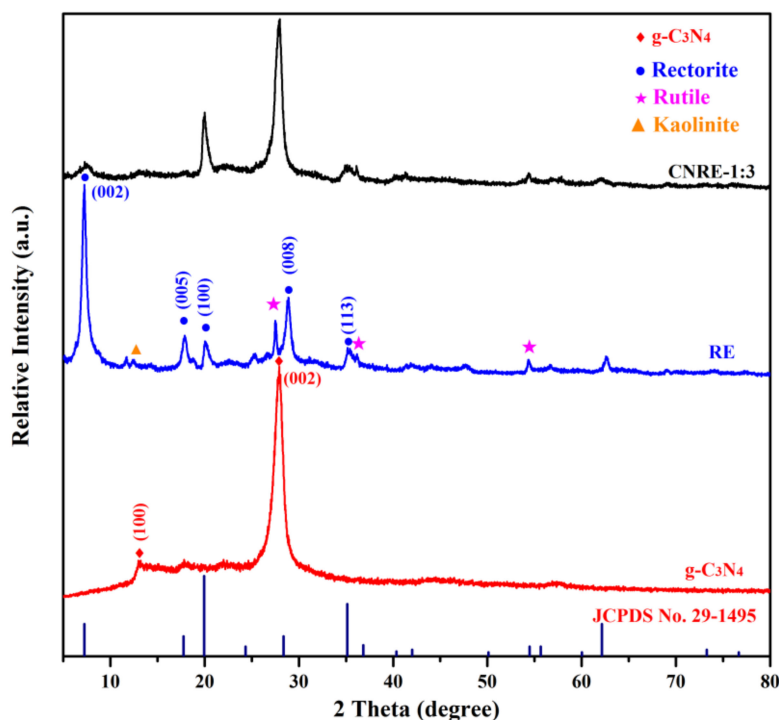


Figure 1. XRD patterns of $g\text{-C}_3\text{N}_4$, rectorite and CNRE-1:3.

3.2. Microstructure Analysis

The microstructures of $g\text{-C}_3\text{N}_4$, rectorite and CNRE-1:3 were investigated with SEM analysis. As displayed in Figure 2a,b, the bare $g\text{-C}_3\text{N}_4$ possessed a typical aggregated layered structure, which should be attributed to the thermal polymerization of dicyandiamide. As seen in Figure 2c,d, the rectorite showed a layered structure composed of parallel nanosheets with a smooth surface. This lamellar structure would benefit for 2D $g\text{-C}_3\text{N}_4$ immobilization. Compared with the pure rectorite, the rougher surface of CNRE-1:3 (Figure 2e,f) could also prove the successful immobilization of $g\text{-C}_3\text{N}_4$ nanosheets on the surface of rectorite. The elemental compositions of CNRE-1:3 were further detected by element mapping in element mapping mode. As can be seen from Figure 2g, it is indicated that the C, N, O, Al, Si are observed in composite and evenly distributed, which demonstrates the well distributions of $g\text{-C}_3\text{N}_4$ on layered rectorite. More importantly, the well distribution of these elements revealed that the coexistence and contact of $g\text{-C}_3\text{N}_4$ and rectorite.

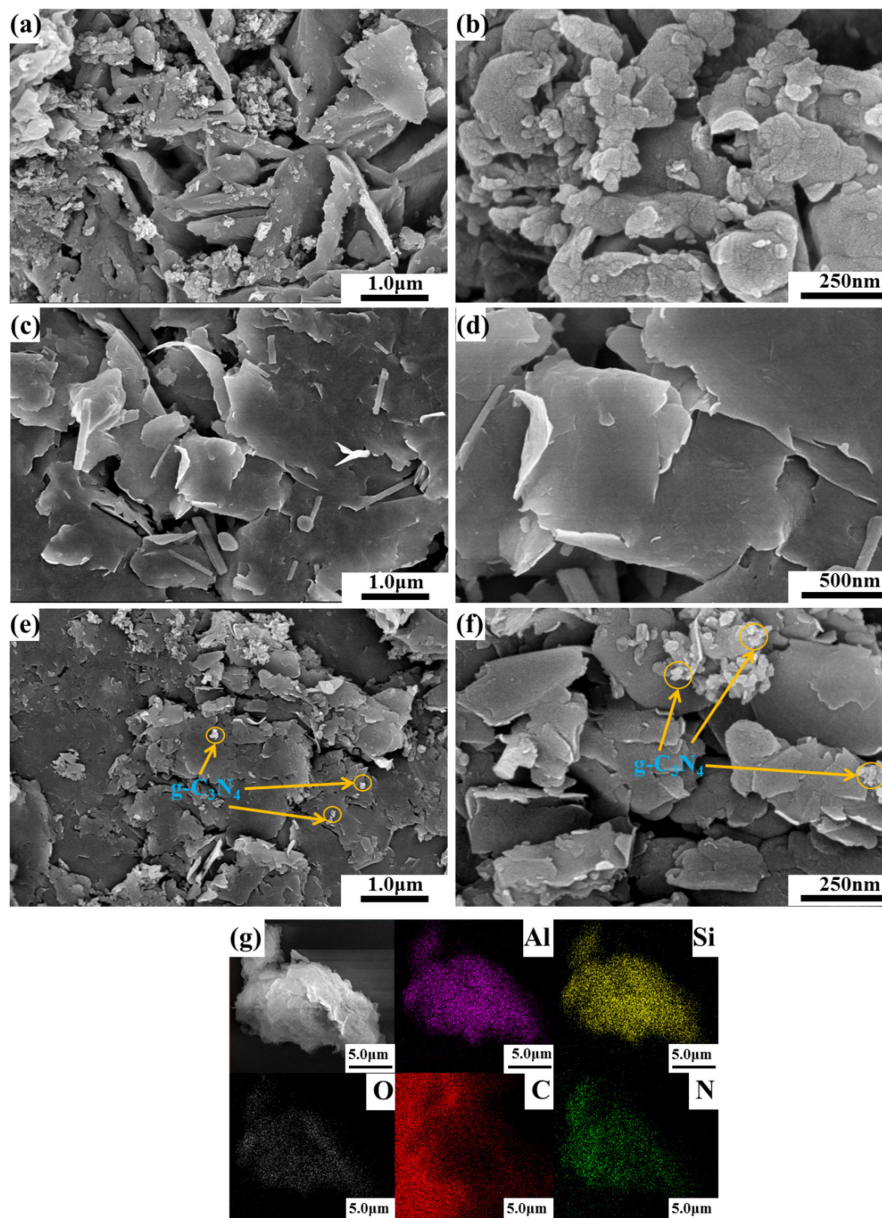


Figure 2. (a,b) SEM images of g-C₃N₄; (c,d) rectorite; (e,f) CNRE-1:3; (g) element mapping of Al, Si, O, C, N for CNRE-1:3 composite.

3.3. Photoluminescence Analysis

The photoluminescence (PL) analysis was generally used to demonstrate the separation and recombination of electron-hole pairs by determining the charge-carrier trapping, transfer capacity of semiconductor under illumination [27]. The typical PL plots of g-C₃N₄ and CNRE-1:3 are observed in Figure 3. It is evidence that g-C₃N₄ displayed the similar peak position with that of CNRE-1:3 composite, observing the maximum peaks at around 450 nm because of band edge and defect emission [28]. However, compared to bare g-C₃N₄, the peak intensity of CNRE-1:3 was significantly decreased due to the introduction of rectorite. Generally, the sample with lower PL intensity stands for the higher separation efficiency of electron-hole pairs [29]. Hence, it is concluded that the immobilization of g-C₃N₄ nanosheets on the surface of rectorite could efficiently suppress the recombination of electron-hole pairs, enhancing the charge transfer in the photocatalytic process.

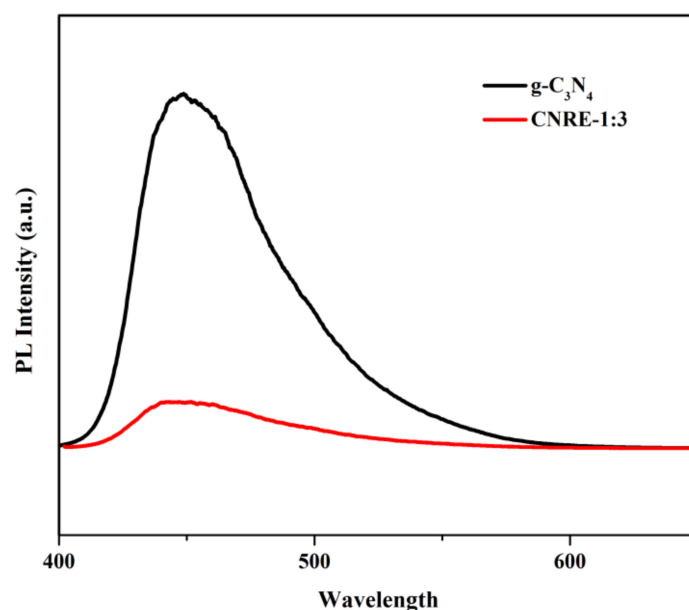


Figure 3. PL emission spectra ($\lambda_{\text{exc}} = 360 \text{ nm}$) of $\text{g-C}_3\text{N}_4$ and CNRE-1:3 composite.

3.4. FTIR Analysis

FTIR spectra of CNRE-1:3, $\text{g-C}_3\text{N}_4$, RE-550 °C and RE were displayed in Figure 4. The $\text{g-C}_3\text{N}_4$ revealed three main absorption regions. The peak at 3000–3500 cm^{-1} was attributed to the stretching vibration of N–H and surface adsorbed water molecules. The peak at 1637 cm^{-1} was due to the presence of C–N bonds and the peaks at 1411 cm^{-1} , 1325 cm^{-1} and 1240 cm^{-1} were assigned to the typical vibration of aromatic rings [30,31]. The absorption peak at 807 cm^{-1} accorded with the characteristic breathing mode of triazine units [32]. For the rectorite, major peaks were in the range of 960–1150 cm^{-1} , which could be ascribed to the Si–O stretching vibration of silica tetrahedron. The peak at 1635 cm^{-1} corresponded to the bending vibration of H_2O . All the main characteristic vibration peaks of $\text{g-C}_3\text{N}_4$ and rectorite could be clearly found in the FTIR spectra of CNRE-1:3, suggesting the structure of $\text{g-C}_3\text{N}_4$ and rectorite remains intact after wet-chemical and calcination processes. However, no newborn functional groups were observed from the FTIR spectra analysis.

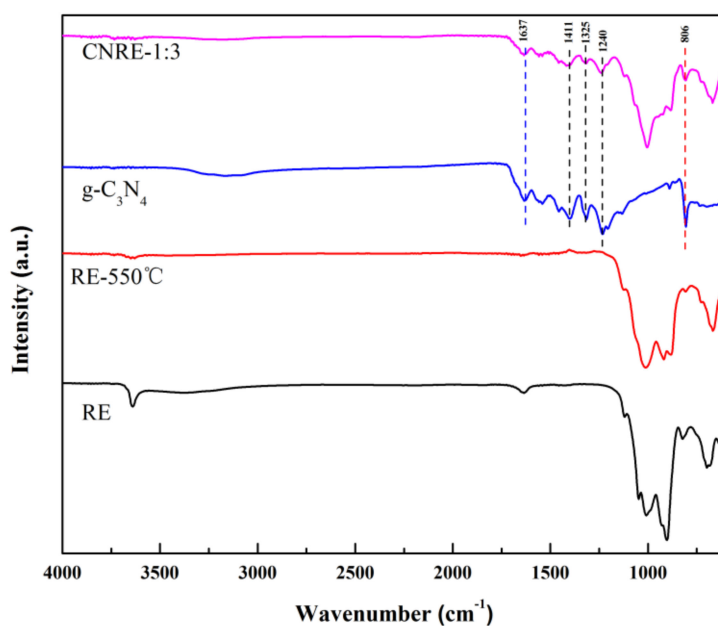


Figure 4. FTIR spectra of CNRE-1:3, $\text{g-C}_3\text{N}_4$, RE-550 °C and rectorite.

3.5. BET Analysis

The surface area and pore structure of RE, $g\text{-C}_3\text{N}_4$ and CNRE-1:3 were investigated by N_2 adsorption-desorption isotherms and Barrett–Joyner–Halenda (BJH) pore size distribution plots. From Figure 5, the nitrogen adsorption-desorption isotherms plots of all samples exhibited a type II isotherm and the hysteresis loops were the type of H3, which typically present the formation of mesoporous structure with the pore size of 2–50 nm. As shown in Figure 5a,c, the pore size of CNRE-1:3 was similar with the RE, which demonstrated the introduction of $g\text{-C}_3\text{N}_4$ had almost no influence on the porous structure of rectorite. As presented in Table 1, the surface area of CNRE-1:3 and rectorite had almost the same surface area. It could be inferred that the structure of rectorite might not be destroyed during the calcination process at 550 °C. However, the surface area and pore volume of CNRE-1:3 were larger than those of $g\text{-C}_3\text{N}_4$, which would be beneficial for generating more adsorption and reactive sites for pollutant degradation.

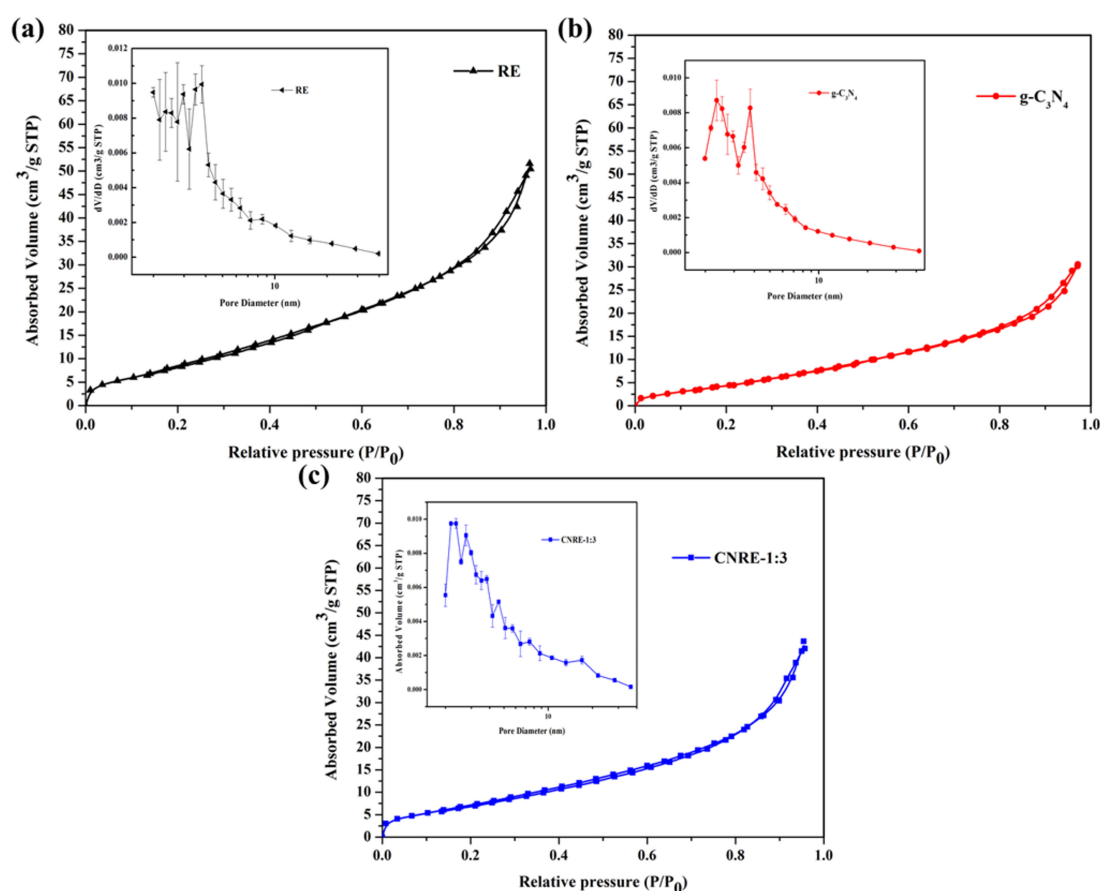


Figure 5. N_2 adsorption-desorption isotherms measured at 77 K as well as BJH pore size distribution plots of (a) rectorite, (b) $g\text{-C}_3\text{N}_4$ and (c) CNRE-1:3.

Table 1. N_2 adsorption-desorption characteristics of the rectorite, $g\text{-C}_3\text{N}_4$ and CNRE-1:3 composite.

Sample	\bar{S}_{BET} (m ² /g)	Standard Deviations of S_{BET}	Pore Volume (cm ³ /g)
Rectorite(RE)	28.9	1.3	0.060
$g\text{-C}_3\text{N}_4$	16.2	2.2	0.046
CNRE-1:3	27.1	1.5	0.062

3.6. Photocatalytic Activity

In this work, CIP was employed as the target pollutant to determine the photoactivity of samples. The photocatalytic activities of rectorite, $g\text{-C}_3\text{N}_4$, CNRE-1:1, CNRE-1:2, CNRE-1:3, CNRE-1:4 and

CNRE-MIX were revealed in Figure 6. As described in Figure 6a, interestingly, the removal rate of CIP was only about 12.3% after adsorption by pure $g\text{-C}_3\text{N}_4$, which was mainly because of its agglomeration of lamellar nanosheets. As the amount of dicyandiamide increased, the adsorption rate of $g\text{-C}_3\text{N}_4$ /rectorite raised gradually and then decreased. CNRE-1:3 possessed the best adsorption activity and the removal rate of CIP increased to 29.2%. This phenomenon could be attributed to the higher adsorption ability of rectorite as catalyst carrier. In addition, the introduction of rectorite would be beneficial for exfoliation of the stack $g\text{-C}_3\text{N}_4$, which also greatly promoted its adsorption ability towards CIP. After 6 h illumination, it is apparent that in the presence of rectorite, only about 16.3% removal rate for CIP can be obtained because of adsorption. For pure $g\text{-C}_3\text{N}_4$, this value reached about 33.4% ascribed to the photocatalysis of $g\text{-C}_3\text{N}_4$. By contrast, CNRE-1:3 revealed the highest degradation efficiency for CIP (around 70%). Furthermore, the photocatalytic degradation obeyed the first-order kinetics. The kinetics could be denoted as below [15]:

$$-\ln(C_0/C) = kt \quad (2)$$

Based on the first-order kinetics, the rate constants of CNRE-1:1, CNRE-1:2, CNRE-1:3, CNRE-1:4, CNRE-MIX and $g\text{-C}_3\text{N}_4$ were calculated to be 0.00093 min^{-1} , 0.00150 min^{-1} , 0.00215 min^{-1} , 0.00202 min^{-1} , 0.00041 min^{-1} and 0.00038 min^{-1} , respectively. It is clear that the rate constant of CNRE-1:3 was 5.66 times that of single $g\text{-C}_3\text{N}_4$ and 5.24 times that of CNRE-MIX. The introduction of natural rectorite not only increased the degradation efficiency but also reduced the usage of $g\text{-C}_3\text{N}_4$ photocatalyst in practical application. Hence, considering the low cost and abundance of natural rectorite, the as-prepared $g\text{-C}_3\text{N}_4$ /rectorite composite should be an environmentally and economically photocatalytic material in the field of wastewater treatment.

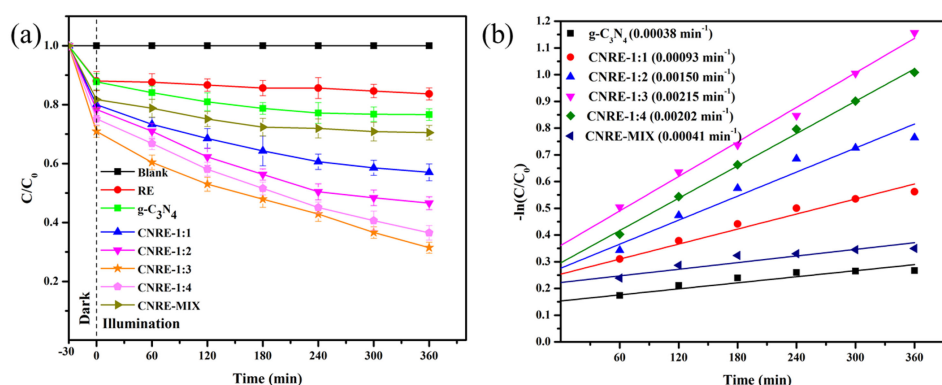


Figure 6. (a) Photodegradation of CIP by rectorite, CNRE-1:1, CNRE-1:2, CNRE-1:3, CNRE-1:4, CNRE-MIX and $g\text{-C}_3\text{N}_4$ under visible light; (b) the corresponding first-order kinetics plots.

3.7. UV-Vis Diffuse Reflection Spectrum

UV-vis diffuse reflectance spectra of rectorite, $g\text{-C}_3\text{N}_4$ and CNRE-1:3 were depicted in Figure 7a. The intensity of optical absorption of rectorite remained higher, which might be due to that the gray rectorite is easier to absorb light. Besides, the bare $g\text{-C}_3\text{N}_4$ revealed the absorption edge at 441 nm, which was in good agreement with the observation of previous literature [33]. Furthermore, the band gap of semiconductor can be determined by the formula $\alpha_{\nu} = A(h_{\nu} - E_g)^{n/2}$ [34], which revealed the band gap of roughly 2.78 eV and 2.73 eV for $g\text{-C}_3\text{N}_4$ and CNRE-1:3, respectively. Compared with single $g\text{-C}_3\text{N}_4$, no obvious enhancement of the absorbance intensity of CNRE-1:3 in visible light region was observed. This should be because the carrier rectorite has no visible light absorption ability. However, the change of optical properties further verified the effective immobilization of $g\text{-C}_3\text{N}_4$ on rectorite. Hence, we can conclude that the performance improvement mechanisms should be the improvement of adsorption capacity towards CIP, the distribution of catalyst and the effective separation of photogenerated electron-hole pairs, rather than extended light harvesting.

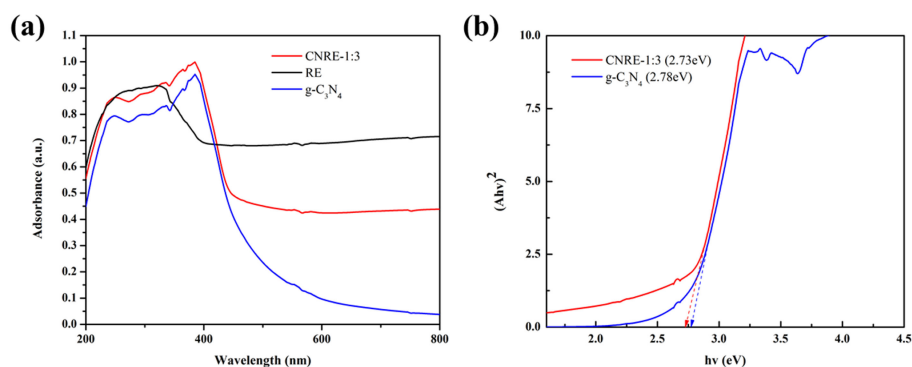


Figure 7. (a) UV-vis spectra; (b) band gaps of rectorite, g-C₃N₄ and CNRE-1:3.

3.8. The Reusability and Stability of Catalyst

In order to further study the reusability and stability of CNRE-1:3, five successive photocatalytic experiments were implemented under the same conditions. However, the initial concentration of CIP remained constant in each cycle. The results were given in Figure 8. As the reuse time increases, the photocatalytic degradation rate showed a slight downward trend, since the degradation intermediates of CIP absorbed on the surface of catalyst, resulting in the decrease of photoelectron transfer [35]. However, compared with initial degradation performance, the photocatalytic activity of CNRE-1:3 still maintains a high level after five successive runs. This means that the CNRE-1:3 has great application potential in wastewater treatment with good reusability and low cost.

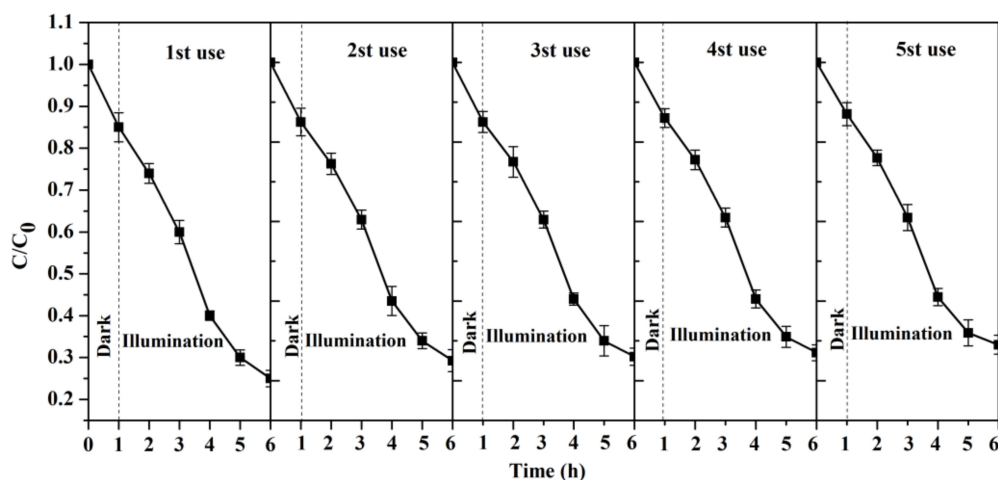


Figure 8. The reusability and stability test of CNRE-1:3.

3.9. Proposed CIP Degradation Pathways

To better understand the degradation processes of CIP by composite, the intermediate products in catalytic reaction process were analyzed and briefly described in Table 2. The intermediates namely P1 ($m/z = 362$), P2 ($m/z = 306$), P3 ($m/z = 291$), P4 ($m/z = 263$), P5 ($m/z = 348$), P6 ($m/z = 288$) and P7 ($m/z = 133$) were reviewed. A representative mass spectra of CIP after 6 h of irradiation was shown in Figure 9. The proposed degradation pathways of CIP by CNRE-1:3 under visible light were revealed in Figure 10. As described in Figure 10, two main decay pathways were presented. The molecular weight of intermediates were apparently decreased in all the pathway, indicating that CIP was decomposed effectively. In pathway I, the piperazine ring was oxidized causing the ring to open. Then, two -CO were lost when P1 transformed into P2 [36,37]. Consulting previous studies [38,39], P3 generated through the processes of hydroxylation and the removal of CHNH₂ from P2. In the following step, the P4 was generated and the -CO was eliminated from the piperazine ring [40]. The growth of a

hydroxyl group should be the possible degradation pathway II. One more hydroxyl group was added to generate P5. P5 turn into P6 because losing water and carboxylic group [41]. Finally, original CIP molecules and intermediate were transformed into P7 and further oxidize to CO₂ and H₂O molecular.

Table 2. Oxidation products of CIP degradation by CNRE-1:3 under visible light irradiation.

Products	Molecular Formula	Structural Formula	<i>m/z</i>	Name
CIP	C ₁₇ H ₁₈ FN ₃ O ₃		332	ciprofloxacin
P1	C ₁₇ H ₁₆ FN ₃ O ₅		362	1-cyclopropyl-6-fluoro-7-(N-(2-formamidoethyl)formamido)-4-oxo-1,4-dihydroquinoline-3-carboxylic acid
P2	C ₁₅ H ₁₆ N ₃ FO ₃		306	7-((2-aminoethyl)amino)-1-cyclopropyl-6-fluoro-4-oxo-1,4-dihydroquinoline-3-carboxylic acid
P3	C ₁₄ H ₁₁ FN ₂ O ₄		291	1-cyclopropyl-6-fluoro-7-formamido-4-oxo-1,4-dihydroquinoline-3-carboxylic acid
P4	C ₁₃ H ₁₁ FN ₂ O ₃		263	7-amino-1-cyclopropyl-6-fluoro-4-oxo-1,4-dihydroquinoline-3-carboxylic acid
P5	C ₁₇ H ₁₈ FN ₃ O ₄		348	1-cyclopropyl-6-fluoro-2-methyl-4-oxo-7-(piperazin-1-yl)-1,4-dihydroquinoline-3-carboxylic acid compound with λ ¹ -oxidane (1:1)
P6	C ₁₆ H ₁₈ FN ₃ O		288	1-cyclopropyl-6-fluoro-7-(piperazin-1-yl)quinolin-4(1H)-one
P7	C ₉ H ₈ O		133	1-phenylprop-2-en-1-one

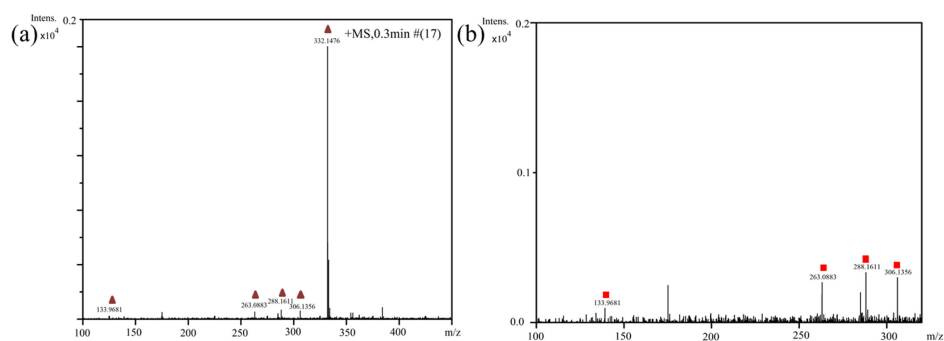


Figure 9. (a) Representative mass spectra of CIP; (b) magnified mass spectra from 0 to 0.2 of intensity.

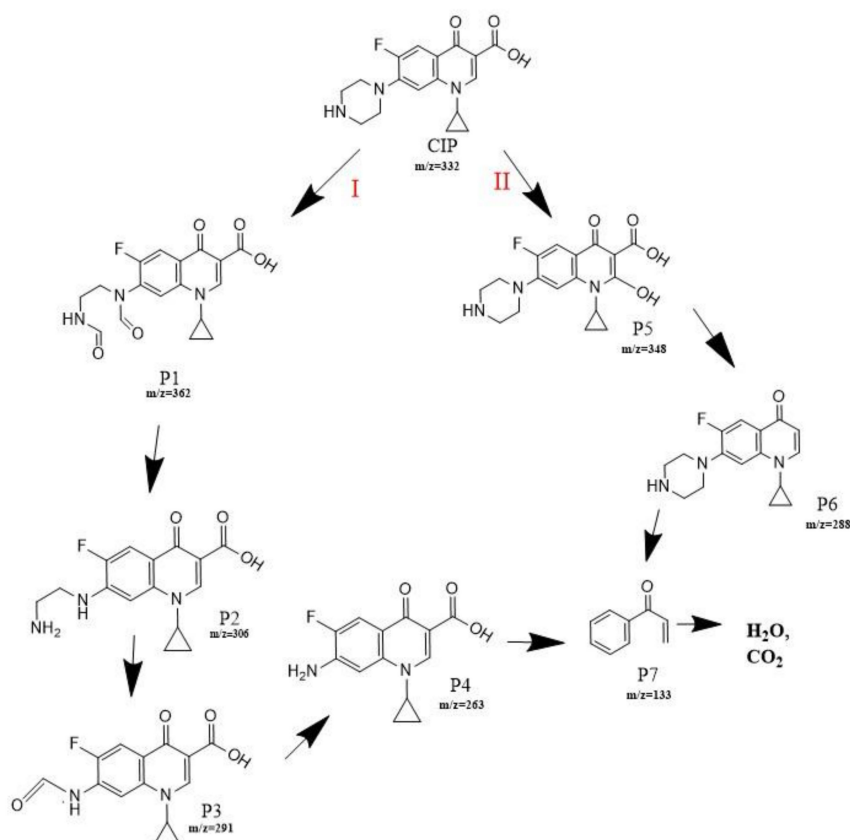


Figure 10. Proposed degradation pathways of CIP by CNRE-1:3 under visible light irradiation.

3.10. Photocatalytic Mechanism

Since the photocatalytic reaction is tightly related to active species, the free radical experiments has been used to further investigate the degradation process and study the photocatalytic mechanisms. The experimental processes were the same as the photocatalytic activity tests except for adding 10 mM of silver nitrate (AgNO_3), edentate disodium (EDTA-2Na), isopropanol (IPA) and 1, 4-benzoquinone (BQ). EDTA-2Na can be used to scavenge h^+ , AgNO_3 was regarded as the scavenger of e^- and BQ was applied to scavenge $\bullet\text{O}_2^-$ and IPA as $\bullet\text{OH}$ scavenger. According to Figure 11, when the BQ and AgNO_3 were added, the degradation efficiency was barely depressed, demonstrating $\bullet\text{O}_2^-$ and e^- radicals were not the dominant reactive species in the photodegradation process. Conversely, the trapping of $\bullet\text{OH}$ by IPA inhibited the decomposition of CIP significantly and slight decrease also observed in EDTA (hole scavenger). The results suggested that the degradation should be mainly mediated by hydroxyl radicals and holes. For bare $\text{g-C}_3\text{N}_4$, the frequent recombination of photo-generated electrons and holes result in a lower activity. The probable photocatalytic mechanism for CNRE-1:3 was depicted in

Figure 12. After the immobilization of stacking $g\text{-C}_3\text{N}_4$ on rectorite, the adsorption capacity towards CIP of catalyst would be improved. On the other hand, the introduction of rectorite significantly improved the distribution of the $g\text{-C}_3\text{N}_4$ nanosheets, which would supply more reactive sites for photodegradation. Furthermore, the formation of the $g\text{-C}_3\text{N}_4$ /rectorite composite could effectively promote the effective separation of photogenerated electron-hole pairs in the photocatalytic process.

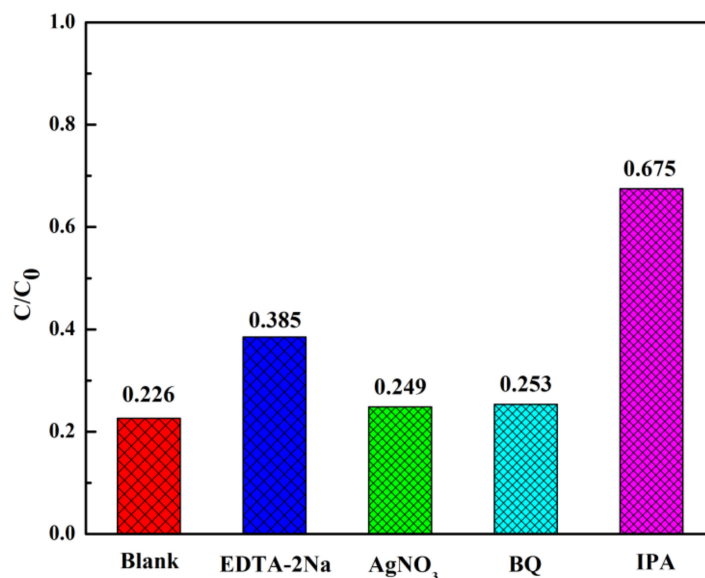


Figure 11. The different effects of active species during photodegradation of CIP.

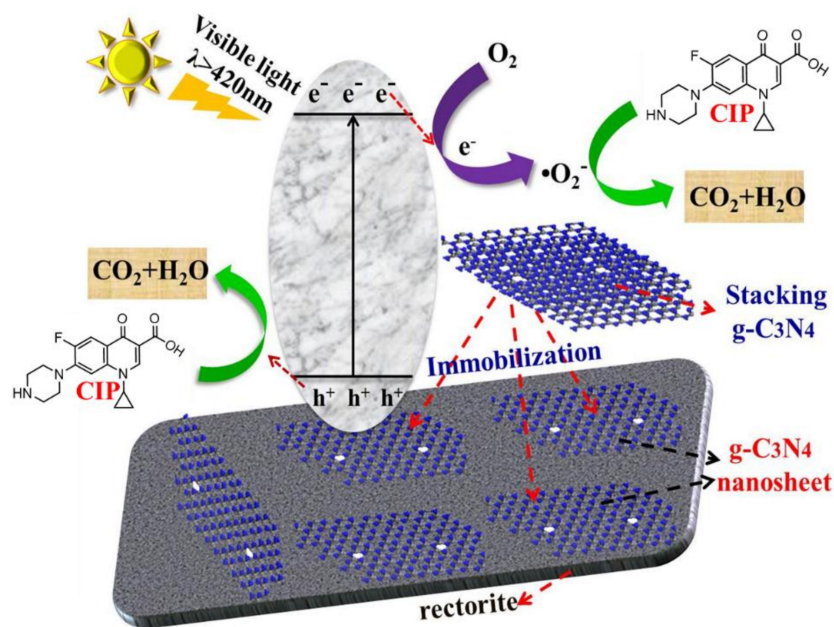


Figure 12. Proposed enhancement mechanisms of $g\text{-C}_3\text{N}_4$ /rectorite composite under visible light.

4. Conclusions

In conclusion, a novel $g\text{-C}_3\text{N}_4$ /rectorite composite was successfully prepared by a facile two-step process. The $g\text{-C}_3\text{N}_4$ was successfully immobilized and uniformly distributed on layered rectorite, generating a novel “2D/2D” structure. Because of the formation of the “2D/2D” structure, the reactive sites for degrading pollutant were increased. Compared with pure $g\text{-C}_3\text{N}_4$, the composite revealed

higher photocatalytic activities and lower recombination of the photogenerated carrier. During the photocatalytic degradation process, it is evidential that the $\bullet\text{OH}$ radicals had the most important effect on the reaction. The reaction rate constant of the prepared g-C₃N₄/rectorite composite is 5.66 times that of bare g-C₃N₄. Based on the structural characterization analysis, the tight interface contact between g-C₃N₄ and rectorite was favorable for decreasing the recombination of e^-h^+ pairs, enhancing the adsorption capacity and photodegradation performance toward the pollutant. The received g-C₃N₄/rectorite composite demonstrate a great potential as a cost-effective photocatalyst for the degradation of personal care products and residuals of medicine in wastewater treatment.

Author Contributions: Conceptualization, Z.S.; Data curation, Z.S. and X.Z.; Funding acquisition, Z.S.; Investigation, Z.S., X.Z., X.D., J.X. and B.W.; Software, X.Z.; Writing—original draft, Z.S., X.Z. and R.Z.; Writing—review & editing, Z.S. and B.W.

Funding: This research was funded by the the Young Elite Scientists Sponsorship Program by CAST (2017QNRC001), National Key R&D Program of China (2017YFB0310803-4), Yueqi Funding Scheme for Young Scholars (China university of Mining & Technology, Beijing), Beijing Excellent Talent Training Subsidy Program–Youth Backbone (2017000020124G089) and Youth Backbone Teacher Growth Support Plan of Beijing Institute of Fashion Technology (BIFTQG201807). The APC was funded by the Young Elite Scientists Sponsorship Program by CAST (2017QNRC001).

Conflicts of Interest: The authors declare no conflict of interest.

References

1. Liu, B.; Guo, W.Q.; Ren, N.Q. Decontamination of wastewaters containing synthetic organic dyes by electrochemical methods: A review. *Adv. Mater. Res.* **2013**, *788*, 405–408. [[CrossRef](#)]
2. Konieczny, K.; Sakol, D.; Bodzek, M. Efficiency of the hybrid coagulation-ultrafiltration water treatment process with the use of immersed hollow-fiber membranes. *Desalination* **2006**, *198*, 102–110. [[CrossRef](#)]
3. Cui, X.; Choo, K.H. Granular iron oxide adsorbents to control natural organic matter and membrane fouling in ultrafiltration water treatment. *Water Res.* **2013**, *47*, 4227. [[CrossRef](#)] [[PubMed](#)]
4. Gupta, V.K.; Kumar, R.; Nayak, A.; Saleh, T.A.; Barakat, M.A. Adsorptive removal of dyes from aqueous solution onto carbon nanotubes: A review. *Adv. Colloid Interface Sci.* **2013**, *193–194*, 24. [[CrossRef](#)] [[PubMed](#)]
5. Lin, S.H.; Lin, C.M. Treatment of textile waste effluents by ozonation and chemical coagulation. *Water Res.* **1993**, *27*, 1743–1748. [[CrossRef](#)]
6. Hassani, A.; Khataee, A.; Karaca, S. Photocatalytic degradation of ciprofloxacin by synthesized TiO₂ nanoparticles on montmorillonite: Effect of operation parameters and artificial neural network modeling. *J. Mol. Catal. A Chem.* **2015**, *409*, 149–161. [[CrossRef](#)]
7. Maeda, K.; Wang, X.; Nishihara, Y. Photocatalytic activities of graphitic carbon nitride powder for water reduction and oxidation under visible light. *J. Phys. Chem. C.* **2009**, *113*, 4940–4947. [[CrossRef](#)]
8. Yuan, Y.P.; Yin, L.; Cao, S.; Gu, L.; Xu, G.; Du, P.; Chai, H.; Liao, Y.; Xue, C. Microwave-assisted heating synthesis: a general and rapid strategy for large-scale production of high crystalline g-C₃N₄ with enhanced photocatalytic H₂ production. *Green Chem.* **2014**, *16*, 4663–4668. [[CrossRef](#)]
9. Lu, X.; Xu, K.; Chen, P.; Jia, K.; Liu, S.; Wu, C. Facile one step method realizing scalable production of g-C₃N₄ nanosheets and study of their photocatalytic H₂ evolution activity. *J. Mater. Chem. A.* **2014**, *2*, 18924–18928. [[CrossRef](#)]
10. Chen, J.; Hong, Z.; Chen, Y.; Lin, B.; Gao, B. One-step synthesis of sulfur-doped and nitrogen-deficient g-C₃N₄ photocatalyst for enhanced hydrogen evolution under visible light. *Mater. Lett.* **2015**, *145*, 129–132. [[CrossRef](#)]
11. Zhang, Y.; Pan, Q.; Chai, G.; Liang, M.; Dong, G.; Zhang, Q.; Qiu, J. Synthesis and luminescence mechanism of multicolor-emitting g-C₃N₄ nanopowders by low temperature thermal condensation of melamine. *Sci. Rep.* **2013**, *3*, 1943. [[CrossRef](#)] [[PubMed](#)]
12. Sehnert, J.; Kilian Baerwinkel, A.; Senker, J. Ab Initio calculation of solid-state NMR spectra for different triazine and heptazine based structure proposals of g-C₃N₄. *J. Phys. Chem. B.* **2007**, *111*, 10671–10680. [[CrossRef](#)] [[PubMed](#)]

13. Liu, H.; Chen, D.; Wang, Z.; Jing, H.; Zhang, R. Microwave-assisted molten-salt rapid synthesis of isotype triazine-/heptazine based g-C₃N₄ heterojunctions with highly enhanced photocatalytic hydrogen evolution performance. *Appl. Catal. B Environ.* **2017**, *203*, 300–313. [[CrossRef](#)]
14. Fan, X.; Xing, Z.; Shu, Z.; Zhang, L.; Wang, L.; Shi, J. Improved photocatalytic activity of g-C₃N₄ derived from cyanamide-urea solution. *RSC Adv.* **2015**, *5*, 8323–8328. [[CrossRef](#)]
15. Ge, L.; Han, C.; Xiao, X.; Guo, L.; Li, Y. Enhanced visible light photocatalytic hydrogen evolution of sulfur-doped polymeric g-C₃N₄ photocatalysts. *Mater. Res. Bull.* **2013**, *48*, 3919–3925. [[CrossRef](#)]
16. Cao, S.; Low, J.; Yu, J.; Jaroniec, M. Polymeric photocatalysts based on graphitic carbon nitride. *Adv. Mater.* **2015**, *27*, 2150–2176. [[CrossRef](#)] [[PubMed](#)]
17. Tunney, J.J.; Detellier, C. Interlamellar amino functionalization of kaolinite. *Can. J. Chem.* **1997**, *75*, 1766–1772. [[CrossRef](#)]
18. Farkas, A.; Dékány, I. Interlamellar adsorption of organic pollutants in hydrophobic montmorillonite. *Colloid. Polym. Sci.* **2001**, *279*, 459–467. [[CrossRef](#)]
19. Dékány, I.; Szántó, F.; Nagy, L.G. Sorption and immersionsal wetting on clay minerals having modified surface. I. Surface properties of nonswelling clay mineral organocomplexes. *J. Colloid Interface Sci.* **1985**, *103*, 321–331. [[CrossRef](#)]
20. Chang, P.H.; Jean, J.S.; Jiang, W.T.; Li, Z.H. Mechanism of tetracycline sorption on rectorite. *Colloids Surf. A.* **2009**, *339*, 94–99. [[CrossRef](#)]
21. Tan, X.L.; Chen, C.L.; Yu, S.M.; Wang, X. Sorption of Ni²⁺ on Na-rectorite studied by batch and spectroscopy methods. *Appl. Geochem.* **2008**, *23*, 2767–2777. [[CrossRef](#)]
22. Zhang, G.; Sun, Z.; Duan, Y.; Ma, R.; Zheng, S. Synthesis of nano-TiO₂/diatomite composite and its photocatalytic degradation of gaseous formaldehyde. *Appl. Surf. Sci.* **2017**, *412*, 105–112. [[CrossRef](#)]
23. Guo, Y.; Yu, W.; Chen, J.; Wang, X.; Gao, B.; Wang, G. Ag₃PO₄/rectorite nanocomposites: ultrasound-assisted preparation, characterization and enhancement of stability and visible-light photocatalytic activity. *Ultrason. Sonochem.* **2017**, *34*, 831–838. [[CrossRef](#)] [[PubMed](#)]
24. Huang, Y.; Ma, X.; Liang, G.; Yan, Y.; Wang, S. Adsorption behavior of Cr(VI) on organic-modified rectorite. *Chem. Eng. J.* **2008**, *138*, 187–193. [[CrossRef](#)]
25. Kabira, I.; Sheppard, L.; Liub, R.; Yaoc, Y.; Zhuc, Q.; Chena, W.; Koshya, P.; Sorrella, C. Contamination of TiO₂ thin films spin coated on rutile and fused silica substrates. *Surf. Coat. Technol.* **2018**, *354*, 369–382. [[CrossRef](#)]
26. Li, C.; Sun, Z.; Zhang, W.; Yu, C.; Zheng, S. Highly efficient g-C₃N₄/TiO₂/kaolinite composite with novel three-dimensional structure and enhanced visible light responding ability towards ciprofloxacin and *S. aureus*. *Appl. Catal. B.* **2018**, *220*, 272–282. [[CrossRef](#)]
27. Zhang, Z.; Long, J.; Xie, X.; Lin, H.; Zhou, Y.; Yuan, R.; Dai, W.; Ding, Z.; Wang, X.; Fu, X. Probing the electronic structure and photoactivation process of nitrogen-doped TiO₂ using DRS, PL and EPR. *ChemPhysChem* **2012**, *13*, 1542–1550. [[CrossRef](#)] [[PubMed](#)]
28. Dong, X.; Sun, Z.; Zhang, X.; Li, X.; Zheng, S. Synthesis and enhanced solar light photocatalytic activity of a C/N co-doped TiO₂/diatomite composite with exposed (001) facets. *Aust. J. Chem.* **2018**, *71*, 315–324. [[CrossRef](#)]
29. Dozzi, M.V.; D'Andrea, C.; Ohtani, B.; Valentini, G.; Selli, E. Fluorine-doped TiO₂ materials: Photocatalytic activity vs. time-resolved photoluminescence. *J. Phys. Chem. B.* **2013**, *117*, 25586–25595. [[CrossRef](#)]
30. Cao, K.; Jiang, Z.; Zhang, X.; Zhang, Y.; Zhao, J.; Xing, R.; Yang, S.; Gao, C.; Pan, F. Highly water-selective hybrid membrane by incorporating g-C₃N₄ nanosheets into polymer matrix. *J. Membr. Sci.* **2015**, *490*, 72–83. [[CrossRef](#)]
31. Huang, S.; Xu, Y.; Xie, M.; Xu, H.; He, M.; Xia, J.; Huang, L.; Li, H. Synthesis of magnetic CoFe₂O₄/g-C₃N₄ composite and its enhancement of photocatalytic ability under visible-light. *Colloids Surf. A* **2015**, *478*, 71–80. [[CrossRef](#)]
32. Tian, J.; Liu, Q.; Asiri, A.M.; Sun, X.; He, Y. Ultrathin graphitic C₃N₄ nanofibers: Hydrolysis-driven top-down rapid synthesis and application as a novel fluorosensor for rapid, sensitive and selective detection of Fe³⁺. *Sens. Actuators B* **2015**, *216*, 453–460. [[CrossRef](#)]

33. Ong, W.J.; Tan, L.L.; Chai, S.P.; Yong, S.T. Graphene oxide as a structure-directing agent for the two-dimensional interface engineering of sandwich-like graphene-g-C₃N₄ hybrid nanostructures with enhanced visible-light photoreduction of CO₂ to methane. *Chem. Commun.* **2015**, *51*, 858–861. [[CrossRef](#)] [[PubMed](#)]
34. Liu, C.; Zhang, Y.; Dong, F.; Reshak, A.H.; Ye, L.; Pinna, N.; Zeng, C.; Zhang, T.; Huang, H. Chlorine intercalation in graphitic carbon nitride for efficient photocatalysis. *Appl. Catal. B Environ.* **2017**, *203*, 465–474. [[CrossRef](#)]
35. Batchu, S.R.; Panditi, V.R.; O’Shea, K.E.; Gardinali, P.R. Photodegradation of antibiotics under simulated solar radiation: Implications for their environmental fate. *Sci. Total. Environ.* **2014**, *470–471*, 299–310. [[CrossRef](#)] [[PubMed](#)]
36. Sutar, R.S.; Rathod, V.K. Ultrasound assisted Laccase catalyzed degradation of Ciprofloxacin hydrochloride. *J. Ind. Eng. Chem.* **2015**, *31*, 276–282. [[CrossRef](#)]
37. Haddad, T.; Kümmerer, K. Characterization of photo-transformation products of the antibiotic drug Ciprofloxacin with liquid chromatography-tandem mass spectrometry in combination with accurate mass determination using an LTQ-Orbitrap. *Chemosphere* **2014**, *115*, 40–46. [[CrossRef](#)]
38. Durán-Álvarez, J.C.; Avella, E.; Ramírez-Zamora, R.M.; Zanella, R. Photocatalytic degradation of ciprofloxacin using mono- (Au, Ag and Cu) and bi- (Au-Ag and Au-Cu) metallic nanoparticles supported on TiO₂ under UV-C and simulated sunlight. *Catal. Today.* **2016**, *266*, 175–187. [[CrossRef](#)]
39. Chen, F.; Yang, Q.; Wang, Y.; Yao, F.; Ma, Y.; Huang, X.; Li, X.; Wang, D.; Zeng, G.; Yu, H. Efficient construction of bismuth vanadate-based Z-scheme photocatalyst for simultaneous Cr(VI) reduction and ciprofloxacin oxidation under visible light: Kinetics, degradation pathways and mechanism. *Chem. Eng. J.* **2018**, *348*, 157–170. [[CrossRef](#)]
40. Chen, Y.; Wang, A.; Zhang, Y.; Bao, R.; Tian, X.; Li, J. Electro-fenton degradation of antibiotic ciprofloxacin (CIP): formation of Fe³⁺-CIP chelate and its effect on catalytic behavior of Fe²⁺/Fe³⁺ and CIP mineralization. *Electrochim. Acta* **2017**, S0013468617320443. [[CrossRef](#)]
41. Perini, J.A.; Silva, B.F.; Nogueira, R.F. Zero-valent iron mediated degradation of ciprofloxacin—assessment of adsorption, operational parameters and degradation products. *Chemosphere* **2014**, *117*, 345–352. [[CrossRef](#)] [[PubMed](#)]



© 2018 by the authors. Licensee MDPI, Basel, Switzerland. This article is an open access article distributed under the terms and conditions of the Creative Commons Attribution (CC BY) license (<http://creativecommons.org/licenses/by/4.0/>).